IEEE Access
Multidisciplinary ⋮ Rapid Review ⋮ Open Access Journal

Received 8 October 2023, accepted 18 October 2023, date of publication 23 October 2023, date of current version 1 November 2023.

Digital Object Identifier 10.1109/ACCESS.2023.3327255

RESEARCH ARTICLE

Spatiotemporal Evolution Law and the Mechanism of Abnormal Surface Deformation in Fault-Affected Mining Zones

XINPENG DIAO[1], QUANSHUAI SUN[1], YAN ZHANG[2], KAN WU[1], JING YANG[3], XIN LU[4], QIUWEN WANG[5], AND JING WANG[1]

[1]School of Environment Science and Spatial Informatics, China University of Mining and Technology, Xuzhou 221116, China
[2]Shandong Provincial Lunan Geology and Exploration Institute (Shandong Provincial Bureau of Geology and Mineral Resources No. 2 Geological Brigade), Jining 272100, China
[3]Geophysical and Geochemical Exploration Institute of Ningxia Hui Autonomous Region, Yinchuan 750021, China
[4]Gucheng Coal Mine, Lu'an Chemical Group Company Ltd., Changzhi 046000, China
[5]School of Foreign Studies, China University of Mining and Technology, Xuzhou 221116, China

Corresponding authors: Yan Zhang (yzhangrn@126.com) and Xinpeng Diao (xpdiao@cumt.edu.cn)

This work was supported in part by the National Natural Science Foundation of China under Grant 52104174, and in part by the Major Research Plan of the Ningxia Hui Autonomous Region under Grant 2022BEG03065.

ABSTRACT Faults are a type of geological structure easily ''reactivated'' by underground mining, which destroys the internal movement and deformation laws of rocks and soil masses and causes anomalous surface sinking features. Therefore, studying the spatiotemporal evolution and deformation mechanism of mining subsidence in regions of fault occurrence is crucial for logical planning of the operating face and preventing and providing early warning of geological disasters. Considering the abnormal surface damage phenomenon in a town in the Hebei Province as the research background, this study used 46 Sentinel-1A radar images from January 3, 2019, to June 26, 2020, to investigate the spatiotemporal evolution of surface movement and deformation during the mining of the working face using the time-series InSAR deformation analysis method. Particularly, a four-threshold permanent scatterer point selection method was proposed and applied to small baseline subset InSAR monitoring. Compared with the monitoring data of 69 benchmarks in the same period, the mean absolute error and root mean square error between InSAR and leveling were 6.7 and 5.3 mm, respectively. These values indicated that the deformation of the mining area inverted by InSAR was reliable. Subsequently, the response mechanism of surface deformation in a region of fault occurrence was analyzed based on separation space theory using a rock beam mechanical model. The results revealed that the abnormal damage area had been deformed since September, 2019, and the abnormal deformation continued to develop with the advancement of the working face. The termination position of the abnormal deformation was approximately linear and relatively spatially independent of the conventional subsidence basin. Additionally, the time-series deformation characteristics of different regions within the influence range of mining were different, and the surface subsidence curve in the direct influence area conformed to the conventional law of subsidence. Surface subsidence in the indirect influence area experienced a process of acceleration and then slowed; the deformation mechanism was different from the conventional movement law of rock strata. The surface outside the affected area exhibited a small uplift, and its active time was consistent with the fault slip instability time. Furthermore, after the fault was disturbed, the rock mass in the fault zone slipped towards the goaf, and a separation space was generated at the fault plane and transferred to the loose layer, which promoted the abnormal expansion of the movement range of overburden and severe deformation at the outcrops. Simultaneously, the footwall of the fault was slightly uplifted owing to the lever principle. Our research results provide data-driven support for the study of abnormal damage laws and the disclosure of their causes. These findings are imperative for the development and improvement of the subsequent subsidence control theory.

The associate editor coordinating the review of this manuscript and approving it for publication was Gerardo di Martino.

INDEX TERMS Fault slip instability, mining subsidence, SBAS-InSAR, separation space.

I. INTRODUCTION

As a basic energy source, coal has long provided a strong guarantee for economic and social development and a safe and stable supply of national energy [1]. However, the large-scale mining of coal resources has also caused significant damage to the ecological environment in mining areas and has led to a series of geological disasters and social issues. Land damage, building/structure damage, mountain collapses, and landslides caused by mining have been frequently reported [2], [3], [4]. The key to reducing or preventing the occurrence of such disasters is clarifying the laws governing mining subsidence. Therefore, scientists have long attached great importance to the study of the law of subsidence, with a series of remarkable achievements [5], [6], [7], [8], [9], [10]. However, the development of coal resources faces complex geological considerations. In particular, the existence of fault structures disrupts the normal patterns of surface movement and deformation distribution, while abnormal surface deformation phenomena continue to occur. Understanding the spatiotemporal evolution and deformation mechanism of abnormal surface deformation in fault-affected mining zones is crucial for effective subsidence control, early warnings for geological disasters, and logical planning for mining operations.

Tectonic faults may cause irregularities in mining subsidence and other surface changes [11]. Many scholars have focused on the phenomenon of abnormal surface damage in subsidence areas caused by faults, performing research on the abnormal damage revealing method, occurrence time, and presentation form. For example, Guo and Dai determined that the fundamental cause of the differential settlement of buildings in Yulin Community, Fushun, was the ''domino'' reaction of local rock mass caused by the interaction between tectonic faults and coal mining subsidence by combining on-site deformation measurement, geological investigation, and structural mechanics analysis [12]. Yu et al., starting from the analysis of the geological and mining conditions in the Pubai mining area, revealed that the reason for many surface cracks and abnormal damage of buildings in Zhangpo Village was the mining-induced fault slip [13]. Xu and Gao analyzed the abnormal surface damage phenomenon in the Dongsheng coal field, Inner Mongolia, finding that even though the existing subsidence theory states that the mining influence boundary will not extend to the fault plane, the surface damage phenomenon will still occur. The stress change around the fault zone can be used as the basis [14] to determine whether the fault is affected by mining subsidence. Ścigała and Szafulera analyzed linear discontinuous deformations on the surface as an effect of underground mining and local geological conditions, suggesting that ground steps occurred as a joined effect of underground mining influences and impact of fault zones located close to the church, likely activated by mining activities [15]. Donnelly comprehensively described the basic situation of coal mining induced fault reactivation in Great Britain [16]; some faults in the settled areas of the U.K. were still characterized by ''activation,'' which would cause serious damage to the surface [17]. However, due to the lack of measured data, it was not possible to determine the duration and spatial distribution of the abnormal deformation.

Currently, the influence of faults on the law of subsidence is mainly thought to be reflected in three aspects: movement range, movement process, and profile shape. The range of surface movement is affected by the nature of the fault, the relationship between the dip angle of the fault plane and movement angle of the rock, and the relationship between the relative position of the fault and goaf. In terms of the profile morphology, there are evident discontinuities and asymmetries in various deformation curves. Swift studied the relationship between joint movement and mining subsidence [18]. Qin et al. studied the ground movement in a mining area with geological faults using FDM analysis and a stacking InSAR method; faults control the spatial extent of the observed ground movement [19]. Zhang et al. studied the law of steep-dip faults on surface deformation caused by underground mining and found that when the fault was located in the compression zone of the surface mining deformation, the probability of discontinuity deformation was reduced; however, when the fault was located in the surface deformation stretching zone, the horizontal movement of the fault outcrop changed significantly, usually manifesting as a tensile fracture [20]. Based on measured surface fracture data, Guo analyzed the morphological characteristics of surface-step fractures under specific fault conditions [21]. Cui et al. discussed a calculation method for steps and fractures at a fault outburst based on the relationship between the dip angle of the fault plane and the movement angle of the bedrock [22]. Xia et al. revealed the mechanisms responsible for mining-induced fault reactivation associated with non-pillar sublevel caving [23]. In addition, some scholars have studied the factors influencing surface movement caused by faults, the sensitivity of fault elements to the law of surface subsidence under different industrial and mining conditions, and the influence of different elements on surface movement and deformation characteristics [24], [25]. However, existing research has mostly analyzed the impact of faults on the final morphology of surface-moving basins from a theoretical or simulated perspective. This has been based on longitudinal profiles, ignoring the development law of movement deformation over time and its cumulative effect on spatial distribution during mining.

To accurately understand the process of surface movement, the research object must be monitored with high precision and reliability. However, abnormal surface deformation and damage are relatively unique and unpredictable and can be easily missed. Furthermore, owing to the shortcomings of traditional surveying methods, such as sparse measurement points, small measurement ranges, and long monitoring periods, long

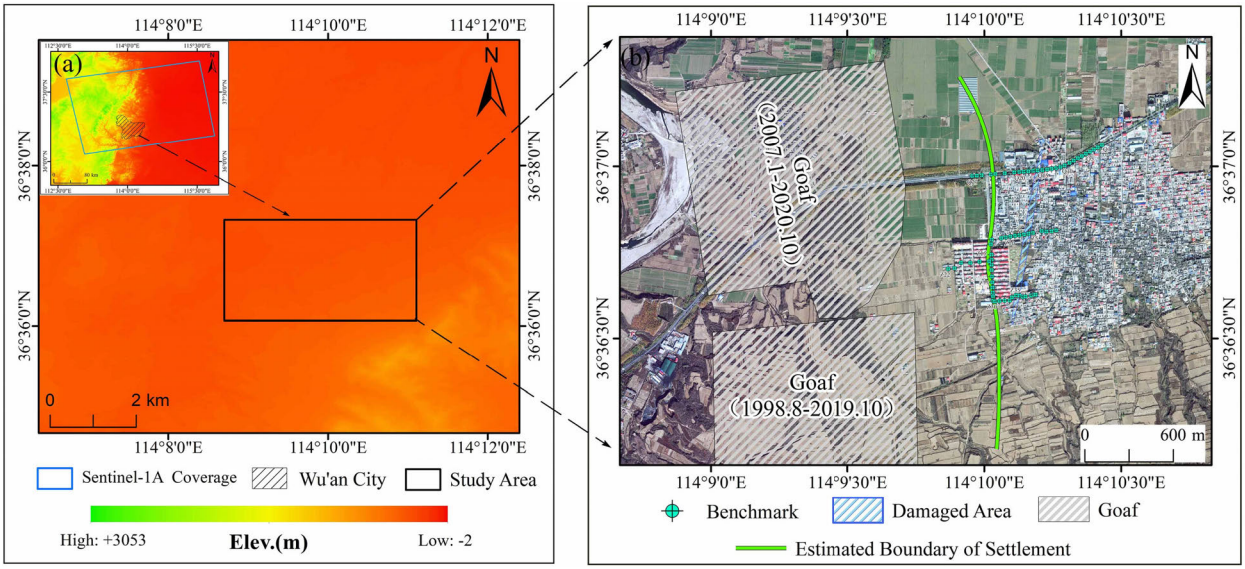

FIGURE 1. Geographical location of the study area: (a) DEM of the study area. (b) Distribution of the goaf and observation points.

time-series multi-dimensional data are lacking [26], [27]. This has contributed to an insufficient understanding of the spatiotemporal evolution characteristics of abnormal surface deformation caused by underground mining. With the continuous enrichment of SAR satellite data and the development of data processing methods, the accuracy of InSAR technology in obtaining surface deformations has reached the millimeter level [28]. Particularly, this technique can be applied to archived images of a study area to invert historical deformation, making it an effective method for studying the law of abnormal surface deformation in fault-affected mining areas.

As the research object in this study, we focused on a town in the Hebei Province. Sentinel-1A images of 46 scenes from January 3, 2019, to June 26, 2020, were used to obtain time-series surface deformation information on the abnormal damage area through an optimized short baseline subset (SBAS-InSAR) technology inversion. Combined with geological data and information on underground mining conditions in the study area, the surface deformation characteristics and spatiotemporal evolution of different locations in the fault-affected mining area were analyzed. Based on the results of the surface deformation analysis, the existence principle of separation space and the rock-beam mechanics model were used to describe the surface deformation mechanism. Our results demonstrate that the SBAS-InSAR technology can effectively identify and extract information on abnormal surface deformation in a fault-affected mining area, providing a data-driven basis for the continued study of this phenomenon. Our research conclusions are conducive to deepening our collective understanding of the laws and characteristics of surface mining deformation in fault-affected areas and have important theoretical and practical significance for the further development and improvement of subsidence control theory, as well as the formulation of relevant protective measures.

II. OVERVIEW OF THE STUDY AREA

A. GEOGRAPHIC LOCATION

The study area is located in the southwest of Handan City, Hebei Province, China, between 113°20'–114°08' E and 37°20'–37°43' N (Figure 1). The terrain in the study area is high in the southeast and low in the northwest, with an altitude of 232–269 m. The land surface was mainly covered by farmland and residential buildings. There are abundant underground coal resources. The total thickness of the coal seam can reach 10 m, and the dip angle of the coal seam is between 5° and 24° with complex geological structural features.

B. MINING DESCRIPTION

Over the past two decades, there has been frequent underground coal mining activity around the study area, and the specific location and distribution of the mined working face are shown in Figure 2a. Fully mechanized mining technology is used to mine the underground working faces. The caving method was used for roof management, and the lithologies of the top and floor of the coal seam were mainly silt-stone. Table 1 lists the mining thickness, depth, size, and other details of the working face.

The geological data of the study area show that there are many faults at this location, among which F13 is the most fully developed. The fault is a tensional reverse fault with a dip angle of approximately 70° and drop of approximately 100 m. The fault locations are shown in Figure 2a. There are protective coal pillars with widths of 40–100 m between the mining working face and faults.

C. SURFACE ABNORMAL DAMAGE PHENOMENON

1) CHARACTERISTICS OF SURFACE DAMAGE

Surface damage to buildings in the study area began to appear in October 2019 and worsened over time. According to this

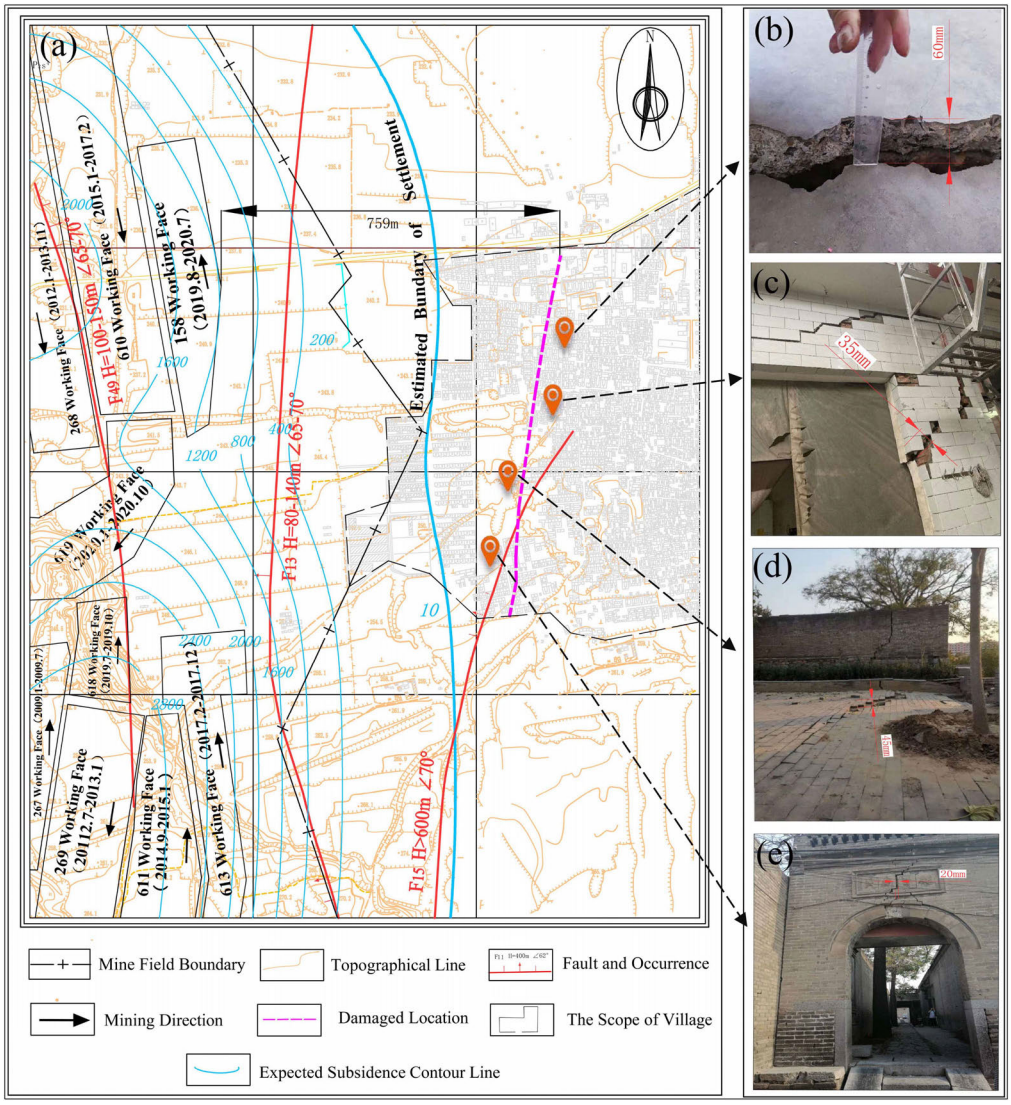

FIGURE 2. Description of the mining situation and damage phenomenon. (a) Location of faults and severely damaged areas. (b–e) Representative photos of house damage.

TABLE 1. Mining information of the working faces around the study area.

No.	Name	Mining Time Span	Mining Thickness m/m	Mining Depth h/m	Coal Seam Dip Angle α/(°)
1	618	2019-07 to 2019-10	4.0	650–700	6
2	158	2019-08 to 2020-07	4.0	750–900	24
3	619	2020-01 to 2020-10	4.0	600–750	17

investigation, the maximum crack width in the building wall reached 30 mm in May 2020. The widths of the ground opening and step cracks were 10–60 mm. The damaged area was distributed in strips, and the specific distribution is indicated by the magenta-dashed curve in Figure 2a. Photographs of the damaged buildings and ground cracks are shown in Figure 2b–e.

2) SUBSIDENCE DAMAGE PREDICTION

Surface deformation caused by underground coal mining is regular, and specific methods can be used to calculate deformation indices. Among these, the probability integral method is one of the most widely used methods for predicting mining subsidence [29], [30], [31]. The probability integral method was used to calculate various surface deformation indices

caused by the mining of the working face, among which the predicted parameters were selected, as listed in Table 2. Figure 2a shows the surface subsidence contours calculated using the probability integral method.

TABLE 2. Predicted parameters of subsidence by probability integration method.

Parameters	Value
Subsidence Coefficient q	0.78
Tangent of Major Influence Angle tanβ	1.70
Propagation Angle of Mining Impact θ (°)	90° - 0.4α
Horizontal Movement Coefficient b	0.30
Inflection Point Offset S (m)	0

The calculation results show that the maximum values of subsidence, tilting, and horizontal deformation within the town were 200 mm, 3.0 mm/m, and 2.5 mm/m, respectively. The mining of underground working faces has caused damage to buildings in the study area. Notably, the degree of damage to buildings caused by underground mining did not exceed Grade II [32], [33], which is inconsistent with the actual damage situation. Additionally, the direct impact boundary of the underground working face (green curve in Figure 1b) did not extend as far as the most severely damaged area of the study site, while the horizontal projection distance between the two exceeded 130 m. This indicates that the damage to residential buildings in the town was abnormal.

III. MATERIALS AND METHODS

To obtain the evolution of surface deformation and elucidate the causes of abnormal surface damage, we used InSAR technology to trace the characteristics of historical surface deformation through archived images and introduced an optimized SBAS time-series analysis method to invert the surface deformation before and after building damage in the study area.

A. MATERIALS

Forty-six Sentinel-1A satellite images from January 3, 2019, to June 26, 2020, were collected to obtain surface deformation information for the study area. The imaging time are listed in Table 3. Additionally, NASA SRTM data with a 30 m resolution were used for the external DEM to eliminate the topographic phase during deformation processing.

B. METHODS

1) SBAS-INSAR

The SBAS technique was proposed to weaken the effects of spatio-temporal decoherence and improve the accuracy of the InSAR surface deformation interpretation. Berardino et al. previously discussed the application of SBAS to surface deformation monitoring [34], [35]. Compared with conventional differential interferometry, the basic idea of the SBAS technique is to group multiphase SAR images in the same

TABLE 3. Relevant Sentinel-1A image parameters of the study area.

Time of Imaging
20190103、20190115、20190127、20190208、20190220、20190304
20190316、20190328、20190409、20190421、20190503、20190515
20190527、20190608、20190620、20190702、20190714、20190726
20190807、20190819、20190831、20190912、20190924、20191006
20191018、20191030、20191111、20191123、20191205、20191217
20191229、20200110、20200122、20200203、20200215、20200227
20200310、20200322、20200403、20200415、20200427、20200509
20200521、20200602、20200614、20200626

study area into several sets of short baselines by setting time and null baseline conditions. The surface deformation time-series of each short baseline set was obtained using the least-squares criterion. The singular value decomposition method was used to jointly solve the grouped short baselines. Subsequently, surface deformation information of the time-series for the entire observation period in the study area was obtained [36].

Specifically, it can be expressed as follows [37], [38]: assuming that the imaging time in the study area is t_0, t_1, t_2 …, for N SAR images of t_{n-1}, M differential interferograms can be formed under the condition of short baseline spacing, and $N/2 \leq M \leq N(n\text{-}1)/2$ can be satisfied. For interferogram i, after removing the flat phase, the interference phase, $\delta\varphi(x, y)$, at any position (x, y) in the interferogram can be expressed as follows:

$$\begin{aligned}\Delta\varphi_i(x,y) &= \delta\varphi_i(t_B,x,y) - \delta\varphi_i(t_A,x,y)\\ &\approx \delta\varphi_{\mathrm{def,i}}(x,y) + \delta\varphi_{\varepsilon,i}(x,y) + \delta\varphi_{\alpha,i}(x,y)\\ &\quad + \delta\varphi_{\mathrm{n,i}}(x,y)\end{aligned} \tag{1}$$

where i represents the interferogram serial number; t_A and t_B are the acquisition times of the SAR image corresponding to interferogram i; $\delta\varphi_{\mathrm{def}}$ is the surface line-of-sight deformation phase in time period $t_A - t_B$; $\delta\varphi_\varepsilon$ is the terrain phase of the target area; and $\delta\varphi_\alpha$and $\delta\varphi_n$represent the atmospheric and noise phases, respectively. The first three terms can be expressed as follows:

$$\begin{cases}\Delta\varphi_{\mathrm{def,i}}(x,y) = 4\pi\left[d_{\mathrm{i}}(t_B,x,y) - d_i(t_A,x,y)\right]/\lambda\\ \delta\varphi_{\varepsilon,i}(x,y) = \left[4\pi\,\Delta z{\cdot}B_\perp(x,y)\right]/(\lambda R sin\theta)\\ \delta\varphi_{\alpha,i}(x,y) = \delta\varphi_{\alpha,i}(t_B,x,y) - \delta\varphi_{\alpha,i}(\mathrm{t}_A,x,y)\end{cases} \tag{2}$$

where $d_i(t_B, x, y)$ and $d_i(t_A, x, y)$ are the surface deformation along the radar line of sight at time t_A and t_B, respectively; λ is the wavelength of the radar; R is the slant range; $B_\perp$ is the vertical baseline; Δ_z is the DEM elevation difference; and θ is the incidence angle. If the deformation rate between different interferograms is $v_{k,k+1}$, the cumulative shape variable between t_A and t_B can be expressed as follows:

$$\Delta\varphi_{\mathrm{def,i}}(x,y) = \frac{4\pi}{\lambda}\sum_{k=t_A}^{t_B-1} v_{k,k+1}\left(t_{k+1} - t_k\right) \tag{3}$$

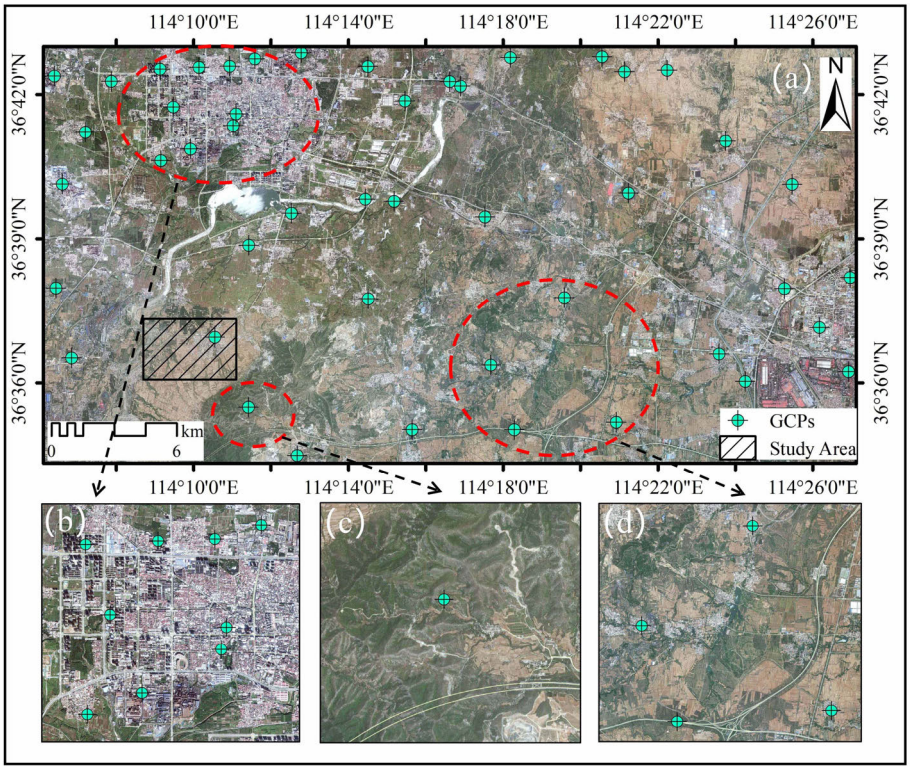

FIGURE 3. Schematic diagram of the GCP distribution. (a) Distribution positions of all GCPs. (b–d) GCPs distributed on buildings (b), bare rock (c), and in villages (d).

After the 3-D space-time phase disentanglement and geocoding of the M interferogram, the deformation rates of different SAR image acquisition times were obtained, and the cumulative deformation information of the surface during the entire observation period was obtained via time integration processing.

2) OPTIMIZED PROCESSING

To eliminate the remaining constant phase in the unwrapped phase map, it is necessary to introduce several Ground Control Points (GCPS) for orbit refinement and interpret the deformation rate and cumulative displacement information based on these points. therefore, the quality of the GCPs directly affects the accuracy of the SBAS deformation interpretation results. Generally, GCPs should be uniformly distributed in a stable area of the surface without a phase jump. Additionally, to allow for their application to most image pairs, a number of GCPs is required. Notably, due to the large surface subsidence gradient of the mining area, high subsidence rate, and incoherent ground pixels, the selection of GCPs using traditional visual interpretation and empirical methods will have a large subjective error.

Permanent scatterers (PSS) can maintain high coherence over long time-series, partially satisfying the GCP selection criteria [39]. Usually, the selection of GCPs is based on the three indicators: the amplitude dispersion index, deformation rate, and coherence coefficient. In consideration of existing research and the characteristics of the mining environment, a four-threshold ps point selection method was proposed for this study; that is, four index thresholds—the three indicators mentioned above and the GCP error—were set, and the qualified PS was used as the final GCP for orbit refinement.

During data processing, the thresholds of the amplitude dispersion index, deformation rate, coherence coefficient, and GCP error were set from 0.2 to 0.4, -0.1 to 0.1, 0.75 to 1, and 0 to 1, respectively. A total of 47 GCPs were selected. When the GCPs were superimposed on the optical image (Figure 3), we found that most of the GCPs were concentrated near towns and attached to artificial fixed objects while a few points were distributed in villages and on roads and bare rock. The location distribution of the GCPs conformed to the selection standard, indicating that the ''four-threshold'' method can be used to select high-quality GCPs, which is conducive to improving the accuracy of the deformation inversion in the study area.

The data processing workflow used in this paper is shown in Figure 4, including the following main steps [40].

(1) Generation of connection graph. The primary image of N interferograms can be different, but the primary and secondary images must be arranged in the same chronological order. When generating the connection graphs, to make full use of the image data, the temporal baseline was set to 60 d, and the spatial baseline was set to 10% of the critical baseline. A total of 215 image pairs were connected, with a maximum

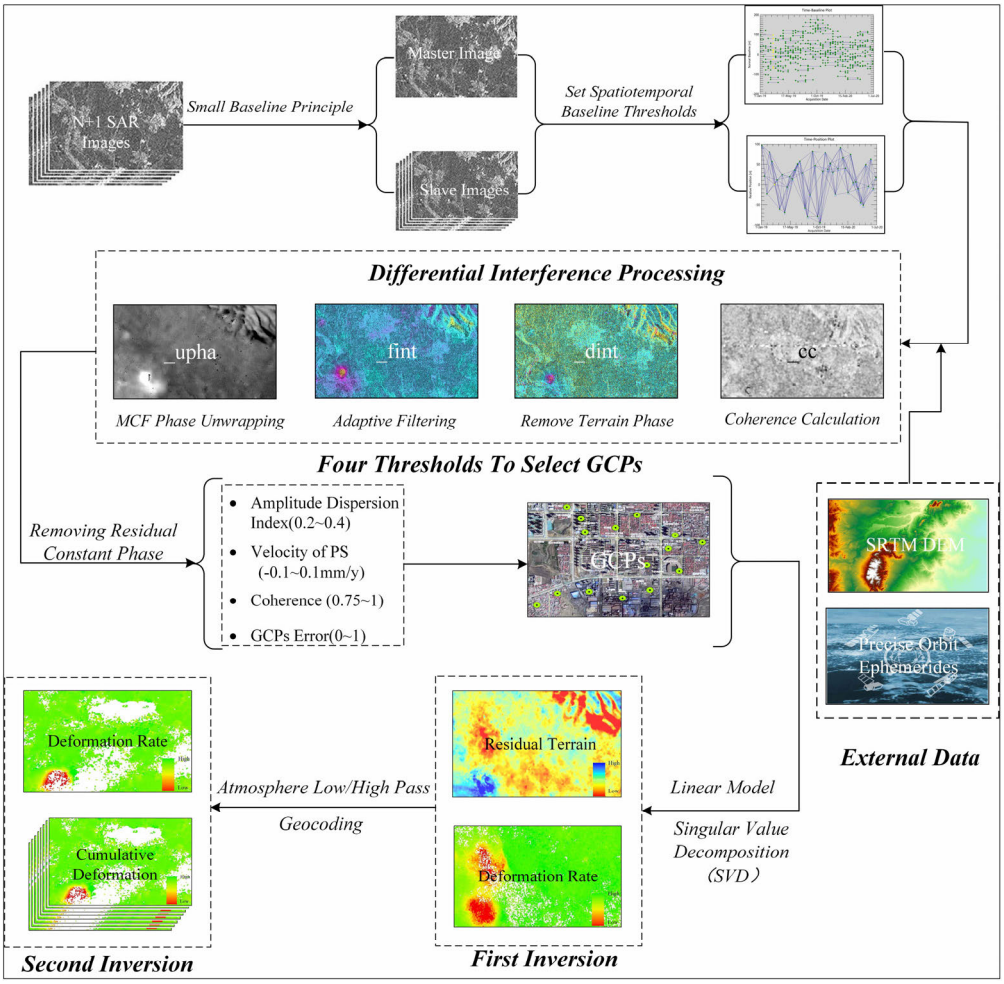

FIGURE 4. Optimized SBAS data processing workflow.

temporal baseline of 60 d and a maximum spatial baseline of 175.72 m (average 55.16 m).

(2) DIfferential interference processing. in the interference processing, the multi-looking ratio between range looks and azimuth looks was set to 4:1 during interference processing. Image registration used the intensity cross-correlation algorithm with precision orbital data to select an adaptive filtering method to remove noise and maintain phase details, and the unwrapping method adopted the minimum cost flow method with the coherence threshold set to 0.3.

(3) Orbital refinement and absolute calibration. To obtain more accurate interference phases, the selected GCPs were used to eliminate orbital errors and residual terrain phases. The GCPs were obtained using the ''four-threshold'' method described above.

(4) Extraction of the deformation time-series. AFter orbital refinement, a more stable linear model was chosen for the first decomposition inversion. Then, with time domain high-pass filtering and spatial domain low-pass filtering, the deformation and deformation rate of the high coherence target points were extracted.

3) MECHANICAL THEORY OF ROCK LAYER CONTROL

According to the mechanical theory of rock layer control, when the mining face does not enter the area affecting the fault, the overburden is not damaged. The two ends of the rock layer belong to a cemented beam structure, as shown in Figure 5a. In the position above the gob, the rock beam exhibits bending and fracture; the two ends of the beam can not only provide horizontal and vertical stress constraints, but also transmit bending moments. With the advance of the working face, when the influence of the change in overburden stress is transmitted to the fault plane, the overburden endpoints near the fault are gradually transformed into a simply supported beam structure because the mechanical strength of the weak fault plane is significantly smaller than that of the overburden, as shown in Figure 5b. A characteristic of this structure is that only the vertical displacement is constrained, and the beam end can rotate freely.

In Figure 5, M_1, M_2, and M_3 are the bending moments of the beam end; q_1 and q_2 are the uniformly distributed load borne by the rock beam; h is the thickness of the rock layer; and L is the span of the beam.

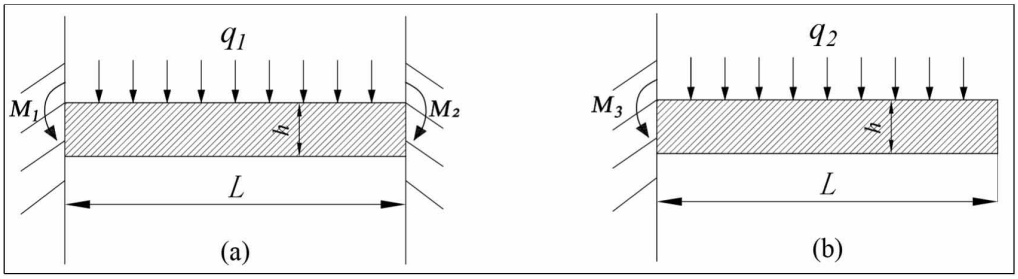

FIGURE 5. Mechanical model of a rock beam. (a) Clamped-clamped beam structure. (b) Distribution of the goaf and observation points.

The maximum bending of the fixed beam, $\boldsymbol{M}_{\mathbf{max1}}$, is at its two ends, and the maximum moment can be expressed as follows:

$$M_{\max 1} = \frac{q_1 L^2}{12} \tag{4}$$

The maximum bending of the simply supported beam, $\boldsymbol{M}_{\mathbf{max2}}$, is at the midpoint position, and the maximum moment can be expressed as follows:

$$M_{\max 2} = \frac{q_2 L^2}{8} \tag{5}$$

The normal stress, σ, at any point on the cross-section of the rock beam in pure bending is:

$$\begin{cases} \sigma = \dfrac{My}{I_Z} \\ I_Z = \dfrac{bh^3}{12} \end{cases} \tag{6}$$

where I_Z represents the moment of inertia of the neutral axis of the rock beam; y represents the distance from the point to the neutral axis; and b and h represent the length and width of the rock beam, respectively.

When the load distributed on the upper part of the rock beam is equal (i.e., $q_1 = q_2$), $M_{\max 1} < M_{\max 2}$ and $\sigma_1 < \sigma_2$. Therefore, the maximum tensile stress of the rock beam was smaller when it did not contain a fault than when it did, indicating that a simple beam was more likely to break than a fixed beam under the same rock formation.

IV. RESULTS AND ANALYSIS

A. VERIFICATION OF INTERPRETATION ACCURACY

Figure 6 shows the three-dimensional distribution of the surface deformation rate obtained through interpretation. The distribution of the vertical surface displacements in different periods indicates the spatial distribution pattern of surface deformation in the study area at different times and their evolution over time, as shown in Figure 7. To verify the reliability of the InSAR interpretation results, the project team collected leveling data from 69 ground observation points from January 5, 2020, to May 3, 2020. The specific distribution of the leveling points is shown in Figure 1b. As we did not obtain leveling data throughout the entire InSAR time series, to reduce the comparison error caused by the difference in timing, we selected InSAR data from January 10, 2020, to May 9, 2020, for comparison. Figure 8a–b shows the deformation curve and comparison of the InSAR and leveling data at each monitoring point. Figure 8c shows a statistical histogram of the difference between the two types of data, and Figure 8d shows the correlation diagram determined by the linear regression method.

Figure 8 shows that the differences between the InSAR and leveling data were mainly concentrated in the range of −5 to +5 mm, and the statistical data conform to a Gaussian normal distribution. The two datasets were linearly correlated ($r^2 = 0.92$), indicating that the deformation trends were consistent. Additionally, the mean absolute error (MAE, θ) and root mean square error (RMSE, σ) between the two datasets were 6.7 and 5.3 mm, respectively, when the leveling data were taken as the most probable value. This further shows that the deformation of the mining area inverted by InSAR is reliable. The spatiotemporal evolution characteristics of the surface deformation can be analyzed based on the InSAR interpretation results.

$$\theta = \frac{1}{n}\sum_{i=1}^{n} |d_{\mathrm{InSAR}} - d_{\mathrm{Level}}| \tag{7}$$

$$\sigma = \sqrt{\frac{1}{n}\sum_{i=1}^{n} (d_{\mathrm{InSAR}} - d_{\mathrm{Level}})^2} \tag{8}$$

where d_{InSAR} and d_{Level} represent the deformation values obtained using InSAR and leveling, respectively, and n represents the number of leveling points.

B. SPATIAL EVOLUTION CHARACTERISTICS OF SURFACE DEFORMATION

The time series diagram of land surface deformation shows the timing of sudden changes on the surface, the dynamic evolution of deformation, and the spatial distribution characteristics. Figure 7a shows that from January 3, 2019, to August 31, 2019, the mining of underground working faces in the surrounding areas did not cause notable deformations in the relevant locations of the town. However, as shown in Figure 7b, surface deformation of the damaged area began to appear at sporadic locations by September 24, 2019, with a value of approximately 10 mm. At this time, the mining of working face 618 was nearing the end, and that of working face 158 was about to be mined, but the buildings had

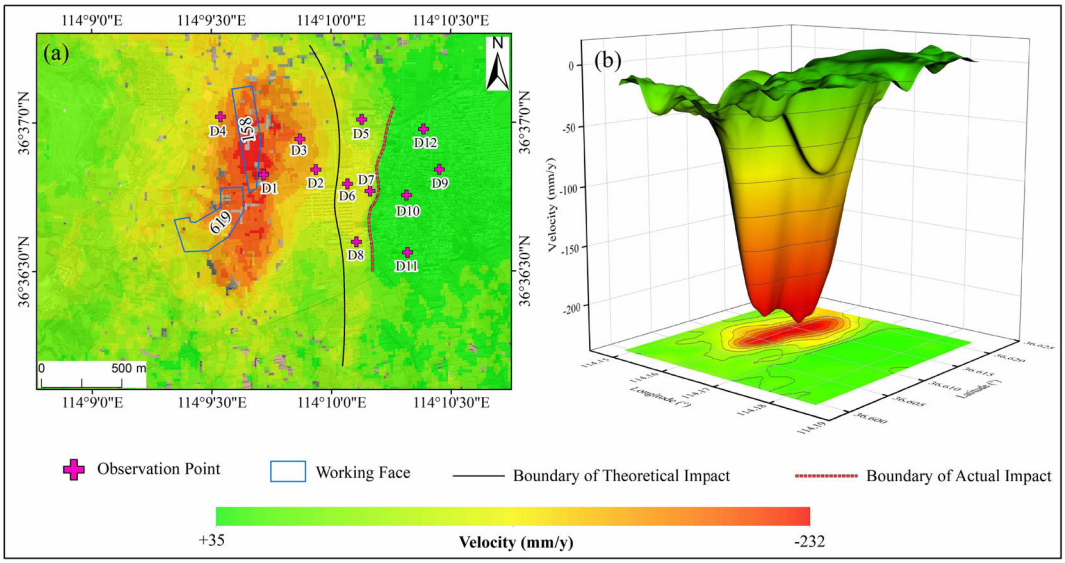

FIGURE 6. Distribution of the surface deformation rate in the study area. (a) Surface deformation rate. (b) Three-dimensional form.

not yet shown notable damage. This indicates that periodic InSAR deformation monitoring can provide early warnings of abnormal surface damage.

Since September 24, 2019, when the advancing distance of working face 158 was approximately 130 m, locations in the town began to exhibit notable surface deformation, the distribution of which was in good agreement with the distribution of severely damaged houses in the town (Figure 7c–f). As shown in Figure 7g–i, in addition to the conventional surface subsidence caused by surface mining at working faces 158, 618, and 619, surface deformation tended to expand to the east, and the terminal position of the spatial development of surface deformation approximately followed a straight-line distribution consistent with the location of abnormal damage in the town, as determined by field investigation.

We observed that the surface deformation at the above locations and the deformation range gradually increased (Figure 7j–k); however, this was independent of the main deformation area caused by the mining of the working face. This is illustrated more intuitively in Figure 6b, which shows the three-dimensional distribution of the surface deformation rate in the study area. Simultaneously, during field investigation we observed that the steps on both sides of the line were sinking (Figure 2b and d). The degree of damage to the houses located there was more severe than that to houses close to the mining area. The spatial distribution pattern and damage characteristics of surface deformation were partially consistent with the law of mining subsidence in a fault-assigned environment.

C. TEMPORAL EVOLUTION CHARACTERISTICS OF SURFACE DEFORMATION

Our analysis in the previous section indicated that the mining of the working face causes the slip instability of surrounding faults, which leads to the expansion of the influence range of surface deformation. To accurately analyze the temporal evolution of surface deformation under the influence of faults, 12 feature points (D1–D12) were selected (Figure 6a). Among them, D1–D4 were located in the area directly affected by the mining of the working face, D5–D8 were located in the area indirectly influenced by fault slip instability, and D9–D12 were located outside of the affected area. The time-series curves of the deformation at each feature point are shown in Figure 9.

1) DIRECT INFLUENCE AREA

The mining influence boundary defined by the probability integral method in Section II-C is regarded as the "theoretical mining influence boundary," and the area west of this line represents the direct influence area. the settlement value at the outermost boundary of the directly affected area is typically 10 mm. Figure 9a shows that no significant surface deformation occurred between January 2019 and July 2019. Mining of working face 618 began in August 2019. Feature point D1, near the opening hole, first appeared in the settlement, and D4 in the old goaf, which is vulnerable to underground mining. In September 2019, the influence of underground mining spread to D2 and D3. Subsequently, the cumulative deformation value of each point continued to increase. The maximum surface settlement near the working face reached 260 mm, and the cumulative surface settlement at the monitoring point furthest from the working face was approximately 110 mm. After February 2020, the mining working face reached full mining capacity, and the settlement rate at each point decreased.

According to the deformation curve characteristics shown in Figure 9a, in the directly affected area, the subsidence curves of each monitoring point conformed to the conventional law of surface subsidence. Fault slip instability caused

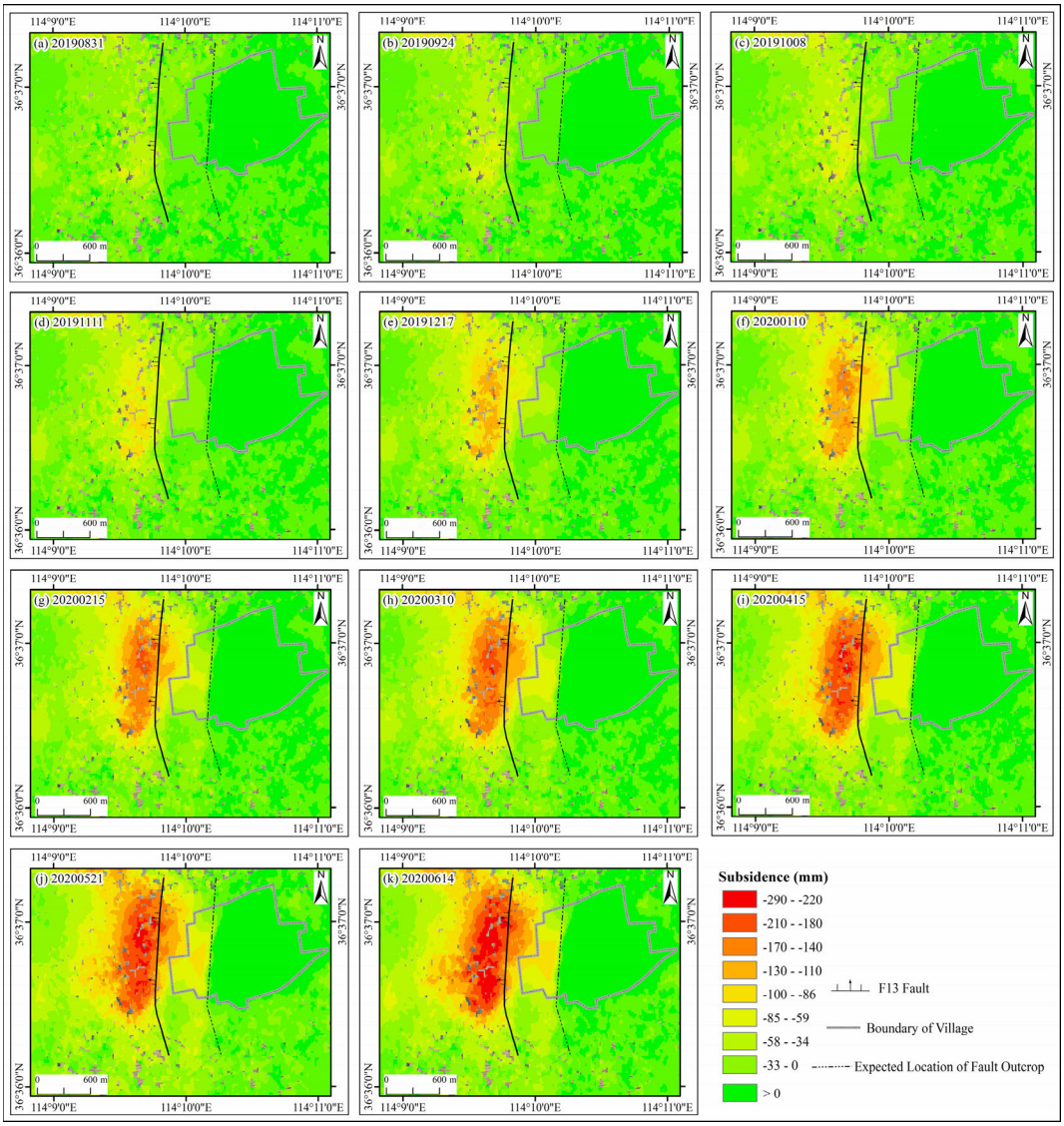

FIGURE 7. Time-series of the surface deformation in the study area.

by mining did not change the characteristics of surface deformation.

2) INDIRECT INFLUENCE AREA

The ''deformation termination line'' detected by INSAR is regarded as the actual mining influence boundary. The area between it and the theoretical mining influence boundary is the surface deformation expansion area caused by fault slip instability, which belongs to the abnormal influence range, is referred to as the indirect influence zone.

As shown in Figure 9b, the indirect influence area, including D6, D7, and D8, was relatively stable before September 2019; this can be regarded as invisible deformation. After September 2019, subsidence began to appear, beginning with a stage of initial acceleration followed by slow deformation. The deformation mechanism differed from the conventional movement law of rock strata. As work advanced northward, D5 began to settle in November 2019 under the influence of fault slip instability. Among the four monitoring points, point D7, which was the farthest from the mining area, settled first and experienced the largest settlement of 105 mm. From the deformation curve, we found that the amount and rate of settlement of D7 and D8, which were farther from the mining area, were greater than those of D5 and D6. The above deformation phenomenon demonstrates that surface deformation begins at the ''deformation termination line'' in the indirect influence area next to the mining area and gradually decreases. Therefore, surface deformation forms two relatively independent subsidence centers in space, as shown in Figure 6b. Additionally, D6 and D8 experienced a new round of acceleration after February 2020, which was related to the onset of mining working face 619 in January 2020, indicating that the activated fault was disturbed once again. Comparing the deformation curves of D5 and D6, we observed that the amount of settlement at D6 was greater than that at D5, which was due to the larger width of the

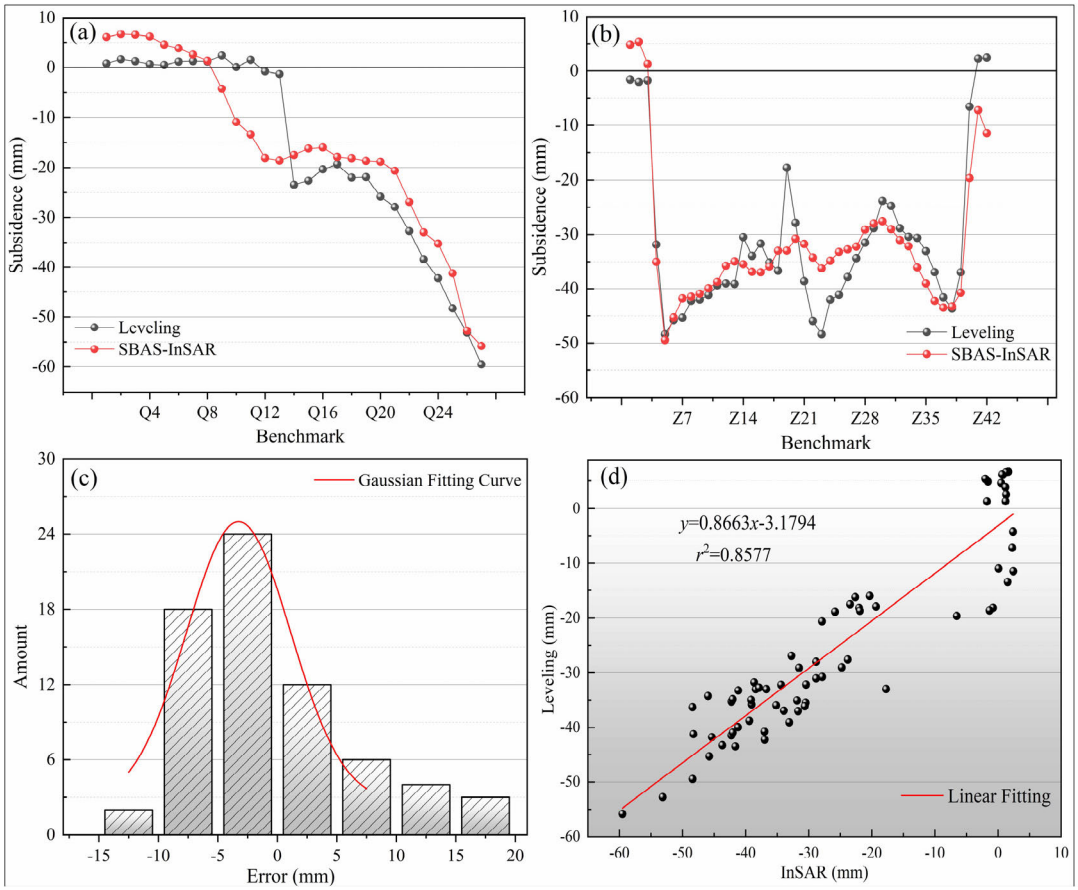

FIGURE 8. Comparison of the InSAR and leveling results of each benchmark. (a–b) Comparison of the InSAR and leveling results. (c) Statistical histogram of the difference between the two types of data. (d) Correlation diagram determined by the linear regression method.

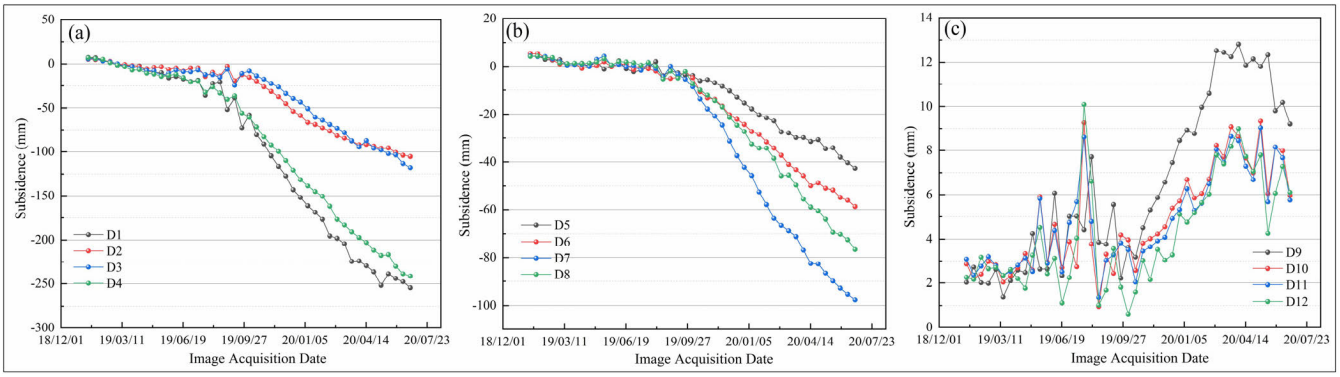

FIGURE 9. Time-series deformation curve of each feature point. (a) Deformation curves of D1–D4. (b) Deformation curves of D5–D8. (c) Deformation curves of D9–D12.

fault-protected coal column at D5 compared to D6. Therefore, the probability of fault disturbances caused by working face mining can be reduced by increasing the width of the fault protection coal pillar.

3) OUTSIDE THE INFLUENCE AREA

Surface subsidence of less than 10 mm is defined as an area not affected by mining. To analyze surface changes outside the mining influence area, four monitoring points, D9–D12, were selected in the area east of the "deformation termination line" extracted by InSAR. The time-series settlement changes at each point are shown in Figure 9c. No significant subsidence was observed at the four monitoring points during the study period. The trends in the time-series monitoring curves for the four monitoring points were consistent. From January 2019 to October 2019, the deformation of each point fluctuated within 1 to 6 mm; this may be considered noise error in the SAR images or the interference of external factors. No significant deformation was identified during this period.

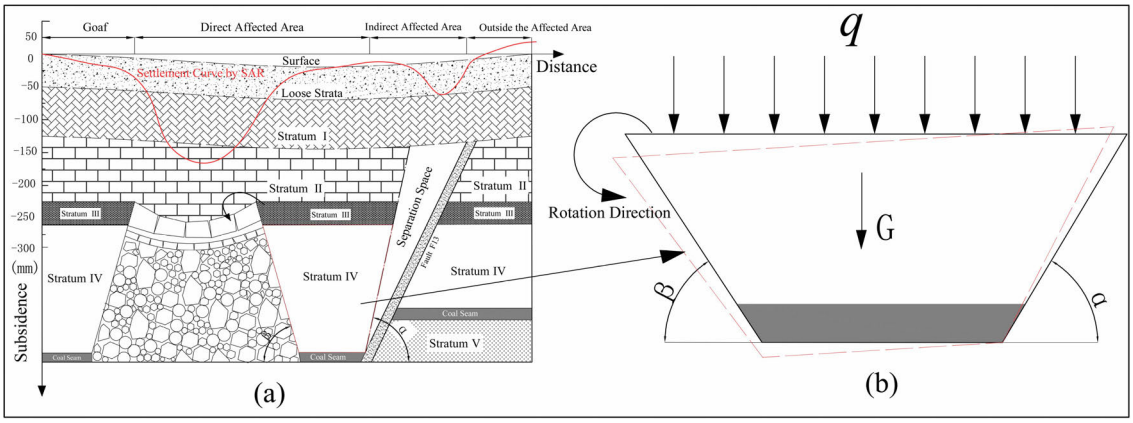

FIGURE 10. Schematic diagram of rock strata movement and stress in the mining area affected by faults. (a) Rock-beam mechanical model. (b) Inverted triangle-shaped separation space.

From November 2019 to March 2020, the four monitoring points experienced different degrees of slow uplift, which coincided with accelerated subsidence at monitoring points D5–D8 in the indirect impact area, after which the ground surface gradually stabilized. Additionally, D9, which was farther from the ''deformation termination line'' had a slightly larger uplift, while D10 to D12 were a similar distance from the ''deformation termination line'' and experienced similar uplift (discussed below).

D. MECHANISTIC ANALYSIS OF SURFACE DEFORMATION

According to an analysis of the upper segment, the fault had an increasing effect on the transmission of surface deformation. Under the influence of faults, surface movement characteristics of different regions differ. To explain this phenomenon, here, we used the mechanical theory of rock layer control to explore the deformation mechanism.

Based on the mechanical theory of rock layer, the free rotation of the beam end cannot be restrained on the fault side. As a result, the tension of the rock beam reaches the breaking limit and breaks under the force of gravity; the collapsed rock spills into the mining area, as shown in Figure 10a.

Figure 10a shows the stress of the rock mass between the goaf and fault. The upper part of the rock mass was evenly distributed, and the internal part of the rock mass was affected by its weight. The right side of the fault was the weak structural plane, and the beam end, as a fixed beam, could rotate freely; on the left side was the bending fault zone of the rock beam. When the dip angle of the fault plane, α, is greater than the collapse angle, β, the rock mass tends to fall to the goaf under the action of the upper load and dead weight, as shown by the dotted line in Figure 10b. There are numerous broken and swollen rock blocks and fractures on one side of the caving zone of the rock mass, which had good compressibility, leading to the recompression of the caved rock and fractures in the gob. This led to the generation of a separation space on the fault side of the rock mass. As there were a large number of broken and rising rock blocks on one side of the rock mass caving zone, the rockfall and fractures in the gob were compressed once again. At this time, an inverted-triangle-shaped separation space was formed between the upper and lower disks of the fault, which was similar to the upper and lower widths, as shown in Figure 10b. The separation space was formed at the fault plane and passed to the loose layer, which aggravated the surface movement and deformation at the fault outcrop and generated a relatively independent settlement area. In contrast, due to the influence of the ''leverage'' effect, the surface experienced a slight ''rebound'' lifting phenomenon due to the increase in the force in the footwall area of the fault.

In summary, we conclude that the disturbance caused by underground coal seam mining to the fault leads to a separation space between the upper and lower walls of the fault, which promotes the expansion of the overburden movement range, thus affecting the surface movement characteristics at different regional locations.

V. CONCLUSION

The mining of underground coal resources causes surface subsidence, which is an important factor leading to secondary geological disasters and environmental damage. The geological conditions in mining areas are complex and often include special tectonics, such as faults. The existence of faults influences the law of surface deformation and causes serious geological damage that is difficult to predict. Therefore, dynamic monitoring of mining subsidence in an area of fault occurrence, study of the spatiotemporal evolution of surface deformation, and clarification of the mechanism of surface deformation have important practical significance for the rational planning of working faces and the prevention and early warning of geological disasters.

In this study, using the optimized SBAS-InSAR method and 46 Sentinel-1A radar images, we retrospectively inverted the deformation spatiotemporal evolution characteristics of the ground surface during the mining of a working face in a town in the Hebei Province. Compared with the leveling

monitoring data in the same period, the MAE and RMSE between InSAR and leveling were 6.7 and 5.3 mm, respectively. This shows that the InSAR interpretation results are reliable.

The spatial evolution of surface deformation revealed that the abnormal damage area had experienced deformation since September 2019. The final morphological characteristics of the spatial distribution of surface deformation were partially consistent with the law of mining subsidence where faults exist. However, the initial location of abnormal deformation was relatively independent of conventional subsidence basins, and then gradually developed into one. According to the spatial distribution pattern of surface deformation, the mining influence area can be divided into three different areas: the direct impact area, indirect impact area, and other locations. In the directly affected area, the settlement curves of the monitoring points conformed to the law of surface subsidence. Fault activation caused by mining did not change the regular characteristics of surface deformation in the area. In the indirectly affected area, surface subsidence experienced an accelerated and then slowed evolution. The surface was affected by mining from the ''deformation termination line'' toward the mining area; the deformation volume gradually decreased. Therefore, the deformation mechanism in this area differed from the regular law of rock movement. A small uplift of the surface occurred at locations outside the impact zone; its active time was consistent with that of fault initiation.

According to the theory of rock formation control mechanics, when the influence of the overburden stress change at the working face is transferred to the fault surface, the overburden endpoints near the fault gradually transform from a fixed beam structure to a simple beam structure. If the dip angle, α, is greater than the caving angle, β, of the fault plane, the rock body will dip in the direction of the mining area under the action of the upper load and self-weight. The rock body produces an inverted triangle-shaped separation space on the side of the fault with a wide top and narrow bottom. The existence of the separation space changes the moving influence range of the overlying rock and the surface moving characteristics of different regional locations.

This study provides preliminary insight into the mechanism of surface mining deformation in a fault-affected environment from the perspective of rock mechanics. Our data provide support for the study of the law of abnormal damage. Our findings are of significance for the development and improvement of subsidence control theory. However, the activation mode of faults caused by mining, the transmission law of movement deformation within the rock mass, and the response mechanism of surface deformation are still not fully understood. These will be the focus of subsequent research through numerical and physical similarity simulations.

ACKNOWLEDGMENT

The authors would like to thank the European Space Agency for providing Sentinel-1A data and also would like to thank the editor and the anonymous reviewers for their valuable suggestions which greatly helped improve the original manuscript.

REFERENCES

[1] F. Liu, W. Cao, J. Zhang, G. Cao, and L. Guo, ''Current technological innovation and development direction of the 14th five-year plan period in China coal industry,'' *J. China Coal Soc.*, vol. 46, no. 1, pp. 1–15, Jan. 2021.

[2] B. Hu, L. Chen, Y. Zou, X. Wu, and P. Washaya, ''Methods for monitoring fast and large gradient subsidence in coal mining areas using SAR images: A review,'' *IEEE Access*, vol. 9, pp. 159018–159035, 2021, doi: 10.1109/ACCESS.2021.3126787.

[3] D. Yang, H. Qiu, S. Ma, Z. Liu, C. Du, Y. Zhu, and M. Cao, ''Slow surface subsidence and its impact on shallow loess landslides in a coal mining area,'' *Catena*, vol. 209, Feb. 2022, Art. no. 105830, doi: 10.1016/j.catena.2021.105830.

[4] M. Yuan, M. Li, H. Liu, P. Lv, B. Li, and W. Zheng, ''Subsidence monitoring base on SBAS-InSAR and slope stability analysis method for damage analysis in mountainous mining subsidence regions,'' *Remote Sens.*, vol. 13, no. 16, p. 3107, Aug. 2021, doi: 10.3390/rs13163107.

[5] B. Ghabraie, G. Ren, J. Barbato, and J. V. Smith, ''A predictive methodology for multi-seam mining induced subsidence,'' *Int. J. Rock Mech. Mining Sci.*, vol. 93, pp. 280–294, Mar. 2017, doi: 10.1016/j.ijrmms.2017.02.003.

[6] H. Zhang, ''Study on equivalent calculation method of surface subsidence in inclined coal seam mining,'' *Coal Sci. Technol.*, vol. 48, no. 10, pp. 119–123, Oct. 2020.

[7] J. Zhang, Y. Yan, H. Dai, L. Xu, J. Li, and R. Xu, ''Hyperbolic secant subsidence prediction model under thick loose layer mining area,'' *Minerals*, vol. 12, no. 8, p. 1023, Aug. 2022, doi: 10.3390/min12081023.

[8] W. Shi, K. Li, S. Yu, C. Zhang, and J. Li, ''Analysis on subsidence law of bedrock and ultrathick loose layer caused by coal mining,'' *Geofluids*, vol. 2021, pp. 1–12, Aug. 2021, doi: 10.1155/2021/8849955.

[9] W. Guo, G. Zhao, E. Bai, M. Guo, and Y. Wang, ''Effect of overburden bending deformation and alluvium mechanical parameters on surface subsidence due to longwall mining,'' *Bull. Eng. Geol. Environ.*, vol. 80, no. 3, pp. 2751–2764, Jan. 2021, doi: 10.1007/s10064-020-02091-4.

[10] W. Yan, J. Chen, Y. Tan, W. Zhang, and L. Cai, ''Theoretical analysis of mining induced overburden subsidence boundary with the horizontal coal seam mining,'' *Adv. Civil Eng.*, vol. 2021, pp. 1–7, Mar. 2021, doi: 10.1155/2021/6657738.

[11] H. Dolezalova, ''Analysis of surface changes from undermining and building site categorization: The case study in mining location Louky near Karvina,'' *Acta Geodynamica et Geomaterialia*, vol. 18, no. 2, pp. 121–135, Mar. 2021, doi: 10.13168/AGG.2021.0009.

[12] X. Guo and J. Dai, ''Analysis of building damage caused by interaction between faults and coal mining subsidence,'' *J. Liaoning Tech. Univ., Natural Sci.*, no. 6, pp. 851–854, Dec. 2006.

[13] X. Yu, G. Huang, B. Zhao, Y. Zhou, and Z. Yang, ''Research on the influence of faults on mining deformation and the method of retaining coal pillars for village protection,'' in *Proc. New Theory Technol. Coal Mining-Acad. Annu. Meeting Mining Prof. Committee China Coal Society*, Liaoning, China, 2010, pp. 11–16.

[14] N. Xu and C. Gao, ''Study on the special rules of surface subsidence affected by normal faults,'' *J. Mining Strata Control Eng.*, vol. 2, no. 1, pp. 101–106, Oct. 2019.

[15] R. Ścigała and K. Szafulera, ''Linear discontinuous deformations created on the surface as an effect of underground mining and local geological conditions-case study,'' *Bull. Eng. Geol. Environ.*, vol. 79, no. 4, pp. 2059–2068, May 2020, doi: 10.1007/s10064-019-01681-1.

[16] L. J. Donnelly, ''A review of coal mining induced fault reactivation in Great Britain,'' *Quart. J. Eng. Geol. Hydrogeol.*, vol. 39, no. 1, pp. 5–15, Feb. 2006, doi: 10.1144/1470-9236/05-015.

[17] L. J. Donnelly, ''Subsidence and associated ground movements on the pennines, northern England,'' *Quart. J. Eng. Geol. Hydrogeol.*, vol. 41, no. 3, pp. 315–332, Aug. 2008, doi: 10.1144/1470-9236/07-216.

[18] G. Swift, "Relationship between joint movement and mining subsidence," *Bull. Eng. Geol. Environ.*, vol. 73, no. 1, pp. 163–176, Feb. 2014, doi: 10.1007/s10064-013-0539-7.
[19] Z. Qin, V. Agarwal, D. Gee, S. Marsh, S. Grebby, Y. Chen, and N. Meng, "Study of ground movement in a mining area with geological faults using FDM analysis and a stacking InSAR method," *Frontiers Environ. Sci.*, vol. 9, pp. 665–2296, Dec. 2021, doi: 10.3389/fenvs.2021.787053.
[20] Y. Zhang, F. Ma, J. Wang, J. Guo, D. Yan, and S. Luo, "Numerical simulation analysis of surface deformation caused by excavation of the upper and lower walls of steep faults," *Chin. J. Geol. Hazard Control*, vol. 23, no. 3, pp. 61–65, Sep. 2012.
[21] W. Guo, "Analysis of the development range and characteristics of surface cracks under the influence of faults," *Mining Saf. Environ. Protection*, vol. 27, no. 2, pp. 25–27, Apr. 2000.
[22] X. Cui, C. Li, D. Yuan, Q. Hu, and C. Ding, "The impacts of weak plane to the surface movement and discontinuous deformation," *J. Hunan Univ. Sci. Technol., Natural Sci. Ed.*, vol. 24, no. 2, pp. 1–4, Jun. 2009.
[23] K. Xia, C. Chen, T. Wang, K. Yang, and C. Zhang, "Investigation of mining-induced fault reactivation associated with sublevel caving in metal mines," *Rock Mech. Rock Eng.*, vol. 55, no. 10, pp. 5953–5982, Oct. 2022, doi: 10.1007/s00603-022-02959-9.
[24] W. Guo, K. Deng, and Y. Bai, "Study on laws of ground surface movements influenced by faults," *J. Liaoning Tech. Univ., Natural Sci.*, vol. 21, no. 2, pp. 713–715, Dec. 2002.
[25] B. Zhao, Z. Liu, W. Wang, and W. Feng, "Analysis of influence of fault activation on protective coal pillar presetting for surface buildings and structures," *Mining Saf. Environ. Protection*, vol. 42, no. 2, pp. 52–59, Dec. 2015.
[26] B. Zhang, S. Wu, X. Ding, C. Wang, J. Zhu, and Q. Li, "Use of multiplatform SAR imagery in mining deformation monitoring with dense vegetation coverage: A case study in the fengfeng mining area, China," *Remote Sens.*, vol. 13, no. 16, p. 3091, Aug. 2021, doi: 10.3390/rs13163091.
[27] X. Diao, Z. Bai, K. Wu, D. Zhou, and Z. Li, "Assessment of mining-induced damage to structures using InSAR time series analysis: A case study of Jiulong mine, China," *Environ. Earth Sci.*, vol. 77, no. 5, pp. 1–14, Feb. 2018, doi: 10.1007/s12665-018-7353-2.
[28] J. Zhu, Z. Li, and J. Hu, "Research progress and methods of InSAR for deformation monitoring," *Acta Geodaetica et Cartograph. Sinica*, vol. 46, no. 10, pp. 1717–1733, 2017.
[29] B. Liu and H. Dai, "Research development and origin of probability integral method," *J. Mining Strata Control Eng.*, vol. 21, no. 2, pp. 1–3, Apr. 2016.
[30] X. Diao, K. Wu, D. Zhou, and L. Li, "Integrating the probability integral method for subsidence prediction and differential synthetic aperture radar interferometry for monitoring mining subsidence in fengfeng, China," *J. Appl. Remote Sens.*, vol. 10, no. 1, Mar. 2016, Art. no. 016028, doi: 10.1117/1.JRS.10.016028.
[31] G. Chen and D. Yang, "A unified analysis framework of static and dynamic structural reliabilities based on direct probability integral method," *Mech. Syst. Signal Process.*, vol. 158, Sep. 2021, Art. no. 107783, doi: 10.1016/j.ymssp.2021.107783.
[32] X. Diao, K. Wu, D. Zhou, J. Wang, Z. Duan, and Z. Yu, "Combining subsidence theory and slope stability analysis method for building damage assessment in mountainous mining subsidence regions," *PLoS ONE*, vol. 14, no. 2, Feb. 2019, Art. no. e0210021, doi: 10.1371/journal.pone.0210021.
[33] Administration of Work Safety, Nation Coal Mine State Administration and National Energy Administration, National Railway Administration of the People's Republic of China, "Mining of building pressure coal," in *Specification for Coal Pillar Retention and Coal Mining in Buildings, Water Bodies, Railways, and Main Tunnels*, 2nd ed. Beijing, China: China Coal Industry Press, 2017, pp. 5–7.
[34] P. Berardino, G. Fornaro, R. Lanari, and E. Sansosti, "A new algorithm for surface deformation monitoring based on small baseline differential SAR interferograms," *IEEE Trans. Geosci. Remote Sens.*, vol. 40, no. 11, pp. 2375–2383, Nov. 2002, doi: 10.1109/TGRS.2002.803792.
[35] R. Lanari, O. Mora, M. Manunta, J. J. Mallorqui, P. Berardino, and E. Sansosti, "A small-baseline approach for investigating deformations on full-resolution differential SAR interferograms," *IEEE Trans. Geosci. Remote Sens.*, vol. 42, no. 7, pp. 1377–1386, Jul. 2004, doi: 10.1109/TGRS.2004.828196.
[36] P. Tizzani, P. Berardino, F. Casu, P. Euillades, M. Manzo, G. Ricciardi, G. Zeni, and R. Lanari, "Surface deformation of long valley caldera and mono basin, california, investigated with the SBAS-InSAR approach," *Remote Sens. Environ.*, vol. 108, no. 3, pp. 277–289, Jun. 2007, doi: 10.1016/j.rse.2006.11.015.
[37] Y. Chen, S. Yu, Q. Tao, G. Liu, L. Wang, and F. Wang, "Accuracy verification and correction of D-InSAR and SBAS-InSAR in monitoring mining surface subsidence," *Remote Sens.*, vol. 13, no. 21, p. 4365, Oct. 2021, doi: 10.3390/rs13214365.
[38] D. Chen, H. Chen, W. Zhang, C. Cao, K. Zhu, X. Yuan, and Y. Du, "Characteristics of the residual surface deformation of multiple abandoned mined-out areas based on a field investigation and SBAS-InSAR: A case study in Jilin, China," *Remote Sens.*, vol. 12, no. 22, p. 3752, Nov. 2020, doi: 10.3390/rs12223752.
[39] X. Luo, X. Xiang, and Y. Lv, "PS correction of InSAR time series deformation monitoring for a certain collapse in Longli County," *Remote Sens. Natural Resour.*, vol. 34, no. 3, pp. 82–87, Nov. 2022.
[40] X. Diao, K. Wu, R. Chen, and J. Yang, "Identifying the cause of abnormal building damage in mining subsidence areas using InSAR technology," *IEEE Access*, vol. 7, pp. 172296–172304, Feb. 2019, doi: 10.1109/ACCESS.2019.2956094.

XINPENG DIAO received the B.S., M.S., and Ph.D. degrees in geodesy and survey engineering from the China University of Mining and Technology, Xuzhou, China, in 2010, 2013, and 2018, respectively. He is currently an Associate Professor with the School of Environment Science and Spatial Informatics, China University of Mining and Technology. His research interests include the deformation monitoring and mining subsidence and its control.

QUANSHUAI SUN received the B.S. degree in surveying and mapping engineering from the Nanjing University of Information Science and Technology, Nanjing, China, in 2021. He is currently pursuing the master's degree in environmental science and spatial information with the China University of Mining and Technology. His research interest includes interferometric synthetic aperture radar and their applications in mining areas.

YAN ZHANG received the B.S. degree from Shandong Agricultural University, in 2004, and the M.S. degree in geological engineering from the China University of Geosciences, Wuhan, China, in 2017. She is currently a Senior Engineer and the Dean of the Jining Branch of Lunan Geo-Engineering Exploration Institute of Shandong Province (Shandong Provincial Bureau of Geology and Mineral Resources No. 2 Geology Group). Her research interests include investigation and assessment of geological hazards in mines.

KAN WU is currently a Full Professor with the School of Environment Science and Spatial Informatics, China University of Mining and Technology. For over 20 years, he has been engaged in teaching and research in surveying and mapping, mainly focusing on mining subsidence, computer mapping, and computer application system development. He has completed more than ten national, provincial, and ministerial level projects. He has published over 70 academic papers and four monographs.

JING YANG received the B.S. degree in surveying and mapping engineering from the China University of Geosciences, Wuhan, China, in 2009. She was with the Geophysical and Geochemical Exploration Institute, Ningxia Hui Autonomous Region for 14 years. She is currently a senior engineer. Her research interests include deep geological structure exploration, clean energy exploration, and geological disaster monitoring and warning.

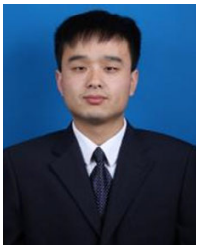

XIN LU received the B.S. degree from Shanxi Agricultural University, Taiyuan, China, in 2012, and the M.S. degree in mining engineering from the China University of Mining and Technology, Xuzhou, China, in 2015. He was with Gucheng Coal Mine, Lu'an Chemical Group Company Ltd. He is currently an engineer. He has been engaged in mining pressure and strata control for eight years.

QIUWEN WANG was born in Chengde, Hebei, China, in 2004. She is currently pursuing the B.S. degree in English major with the China University of Mining and Technology (CUMT), Xuzhou, in 2021. Her research interests include business English, British American literature, and overseas sinology research.

JING WANG was born in Baicheng, Xinjiang, China, in 2003. She is currently pursuing the B.S. degree in surveying and mapping engineering with the China University of Mining and Technology (CUMT), Xuzhou, in 2021. Her research interests include mining subsidence monitoring using InSAR and SAR offset tracking methods.